A software-agnostic benchmark for DEM simulation of cohesive and non-cohesive materials

Mohajeri, M. Javad; Coetzee, Corné; Schott, Dingena L.

DOI
10.1016/j.powtec.2024.120136

Publication date
2024

Document Version
Final published version

Published in
Powder Technology

Powder Technology 447 (2024) 120136

Contents lists available at ScienceDirect

Powder Technology

journal homepage: www.journals.elsevier.com/powder-technology

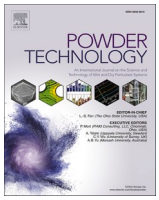

A software-agnostic benchmark for DEM simulation of cohesive and non-cohesive materials

M. Javad Mohajeri [a], Corné Coetzee [b], Dingena L. Schott [a,*]

[a] Department of Maritime and Transport Technology, TU Delft, the Netherlands
[b] Granular Materials Research Group, Department of Mechanical & Mechatronic Engineering, Stellenbosch University, South Africa

HIGHLIGHTS

- This paper provides a framework for software independent DEM simulations.
- The simulations covered free-flowing to cohesive materials.
- Particle level results matched between EDEM and PFC.
- Bulk level results differed with a satisfactory level of agreement.
- Software independent use of calibrated material models should be done with caution.

GRAPHICAL ABSTRACT

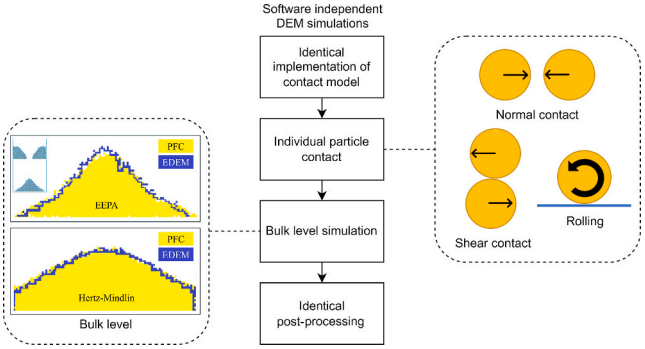

ARTICLE INFO

Keywords:
DEM
Software independent
Benchmark
Calibration
Cohesive
Free-flowing
Particle level
Bulk level
Portability of parameters
Deterministic vs. non-deterministic

ABSTRACT

Although DEM (Discrete Element Method) was introduced >40 years ago, there are still various challenges in applying it with a certain level of confidence. To develop a realistic material model, calibration, validation, particle shape representation and scaling are well-known challenges that have been studied by various researchers over the past two decades. In addition, once a realistic DEM material model is developed and published in line with open science principles, it is unknown to what extent the calibrated values can be used across software packages. Although a benchmark between 8 open source codes was recently published, it did not cover cohesive materials, rolling friction models, realistic calibrated material behaviour, and commercial software that is widely used in industries.

The aim of this study is to investigate the portability of input parameters between different codes and to identify if software independent calibration is possible. We propose a framework to assist DEM users in industry and academia to reach a software independent DEM simulation when required.

To compare the results between software packages, the framework considers the following aspects: 1) identical implementation of contact models, 2) single contact modelling, 3) bulk level simulation, and 4) identical post-processing. This framework is demonstrated for two contact models (Hertz-Mindlin and Edinburgh Elasto Plastic Adhesive) with rolling friction model and two commercial software packages (EDEM and PFC) but is applicable for any other (open-source) software. Moreover, two realistic calibrated material models are included to cover a range of material characteristics, from free-flowing incompressible materials to cohesive compressible

* Corresponding author.
E-mail address: d.l.schott@tudelft.nl (D.L. Schott).

https://doi.org/10.1016/j.powtec.2024.120136
Received 18 May 2024; Received in revised form 26 July 2024; Accepted 29 July 2024
Available online 31 July 2024

materials. This study shows that individual particle level simulations give identical results, bulk level simulations show differences for both contact models. In general, users should use parameter values from other software packages with caution, especially where critical or sensitive applications are modelled. This paper also highlights the use of novel computation techniques, such as the GPU engine, to achieve practical computation times when modelling industrial applications.

1. Introduction

The Discrete Element Method (DEM) is a numerical approach used for the modelling of granular materials. In DEM, individual particles are modelled as discrete elements and contact models are used to resolve the forces and moments acting at particle-particle and particle-wall contacts. DEM can accurately model the characteristics of granular materials under static and dynamic conditions. Once an industrial application is accurately simulated using DEM, simulation-based optimization methods, such as meta-heuristic and surrogate modelling can be applied to enhance a product or process [1,2,6].

DEM is typically used in the food, pharmaceutical, agricultural and mining industries. Here the interest is in bulk materials handling during storage, transportation and processing. Examples include the transport of material on conveyor belts and through transfer chutes [3–5], the interaction with equipment such as excavators and grabs [1,6,7], particle mixing and blending [8,9], and particle breaking or crushing [10].

In these industries and applications, the focus is on accurately modelling and predicting the bulk behaviour of the material, and not necessarily the behaviour of individual particles. This approach allows for a number of simplifications and assumptions to be made to speed up the computation time, especially when large scale industrial applications with billions of particles are analysed. For example, the particle shape can be simplified [11–14], the particle size can be increased (upscaled or coarse graining, [15]) and the contact stiffness can be reduced (to increase the stable timestep, [16]).

The DEM input parameters are defined at the particle and contact level (meso-scale), which determines how the bulk behaviour (macro-scale) is modelled. The input parameters include, for example, the particle-particle coefficient of sliding friction. This parameter is difficult to measure experimentally, especially if the particles are small and irregular in shape and size. Thus, it has become standard practice to calibrate the input parameters [17]. During the calibration process, a laboratory experiment is conducted in which the material bulk behaviour is observed and measured, such as the angle of repose for example. The experiment is then repeated in DEM, and the input parameters adjusted until the bulk behaviour matches that of the experiment. Depending on the number of parameters that need to be calibrated, more than one calibration experiment is usually needed to identify a unique set of parameter values [18].

The calibration of DEM models has been investigated by several researchers and applied in many applications, as reviewed by Coetzee [19]. However, when different software packages are used, it is not guaranteed that the input parameter values calibrated with one package, would provide identical results in another package. Researchers and DEM practitioners often assume parameter values from literature and make use of it without first investigating possible differences in how the parameters are used or implemented in the different software packages.

The contact models can be complex with seemingly small differences in implementation, even when the basic theoretical formulations are identical. However, these small differences in implementation can lead to large differences at the bulk level. Contact detection is a major component of any DEM code and up to 90% of the computation time can be attributed to contact detection and force resolution [20,21]. The software packages make use of different algorithms and implementations to efficiently detect contact and to perform the overlap distance, area or volume calculations. There can also be differences in the time integration schemes employed by different packages, which, even if identical timesteps are used, can result in different results.

For other numerical methods, such as the Finite Element Method (FEM), numerous studies compared different software packages and developed benchmark problems (see for example, [22–27]). However, comparisons between different DEM packages, including open-source, in-house, and commercial codes, are very limited. Since the introduction of DEM in the late 1970's, less than a handful of studies have been published where DEM packages were directly or indirectly compared or benchmarked against analytical results.

The variance and sensitivity of results provided by different analysts and/or simulation packages for the same problem, can be determined through a so-called blind round robin test. These tests are not a direct comparison between software packages since the analysts can freely choose the specific model details which they think would be the most accurate. Several such studies have been published for FEM as discussed by Saomoto et al. [28]. However, the authors are aware of only two round robin studies involving DEM simulations. Holst et al. [29] asked analysts to model the filling of two silos (a model scale and a full-scale) with a well-defined granular material and to report the material free-surface profile, the stress state in the material and the forces on the silo wall. A total of 16 groups of researchers responded using either PFC2D, derivatives of the TRUBAL code, or in-house academic codes developed at universities. It was concluded that “the discrepancy in the results submitted is much greater than first anticipated”. For example, the difference in the wall pressure predictions by the various analysts varied by one order of magnitude. At the time, the variation in results could be partly attributed to the maximum number of particles limited to 10,000 for computational reasons, resulting in a relatively low resolution for wall pressure predictions for example. However, they also concluded that “apparently small changes” in the way that the analysts formulated the problem and created the model, could lead to large variation in the results.

A second DEM round robin test has only been recently published by Saomoto et al. [28]. Note that Saomoto et al. [28] might not have been aware of the study by Holst et al. [29], and referred to their own study as “the first ever round robin test on DEM”. However, in this study, simulated angle of repose results were collected from 16 different groups around the world. Although seven different commercial, open-source and in-house DEM codes were used, this was not a direct comparison. An angle of repose test was conducted by the organizing committee, and the details of the experimental setup and materials used were published. Participants then had to calibrate their own models and predict the angle of repose. Thus, participants ended up using different particle shapes, contact models and input parameter values, even in cases where the same software package was used. Both the modelled angle of repose and the calibrated input parameters were then compared. The predicted angle of repose varied significantly, ranging from 29° to 44° with an average of 36°.

Ramirez-Aragin et al. [30] compared the linear cohesion contact model available in the commercial package EDEM, to the simplified Johnson-Kendall-Roberts (SJKR) and modified SJKR (SJKR2) models available in the open-source code LIGGGHTS. The focus was on powder compaction, and a direct comparison between the two DEM codes was not made, but the objective was rather to find similarities between the options available in both codes.

The first direct comparison between open-source DEM frameworks, that the authors are aware of, was recently published by Dosta et al. [31]. A total of 8 open-source frameworks were compared using

identical input, including initial particle positions, a single contact model (Hertz-Mindlin) and (arbitrary) parameter values. The tests included a single contact analysis of the impact between two particles and a particle against a wall. Further comparisons were based on three case studies of typical DEM applications, namely silo discharge, a rotating drum, and a single particle impacting on a bed of particles. The predicted silo mass flow rate varied by approximately 5%, and the results from the other tests mostly showed levels of variance that one would expect from such models. However, in some cases one or two of the codes predicted results out of line with the majority. In some cases, the discrepancies were due to specific differences in implementation (mostly the treatment of tangential contact forces), and in other cases it could not be explained at all. Although the benchmark is comprehensive, its limitations are that it did not cover rolling friction model, cohesive material model, realistic calibrated material behaviour, and commercial software that is widely used in industries and academia.

The authors are aware of only two published studies where a direct comparison between two commercial DEM software packages was conducted. Chung and Ooi [32] developed benchmark tests to verify DEM codes at the contact for spherical particles. The DEM results were compared to analytical solutions obtained from elasticity theory, FEM results and experimental measurements, and included elastic normal impact and oblique collisions. Although the focus of this study was to develop the benchmark tests, two commercial DEM codes, namely PFC3D (Version 3.0) and EDEM (Beta Version) were used. Where the results from these two packages were directly compared the difference was reported to be in the order of 0.1%.

Rahman et al. [33] directly compared the angle of repose modelled with two commercial software packages, EDEM (Version 2.3) and PFC (Version 4.0.187). They did not compare the two packages at particle or contact level, only at bulk level by modelling and comparing the static angle of repose using the Hertz-Mindlin (no-slip) contact model. It was shown that when using the built-in models, which are seemingly identical, totally different results can be obtained (angle of repose of 44° versus 30°) due to differences in the actual implementation. These differences were, however, not analysed at the contact (particle) level.

Chung and Ooi [32] noted that it was unclear whether the numerous DEM codes had been verified against fundamental benchmark problems and that no standard benchmark tests existed for DEM verification. About 13 years later, Salomon et al. [34] observed that despite intensive development of new open-source and commercial DEM codes, theoretical verification at both the particle and bulk levels is rarely performed or documented. Besides the two round robin tests, only three published studies in the past 13 years have benchmarked DEM codes against analytical results or another DEM code. One recent study compared open-source codes [31], and two studies from 13 years ago compared commercial codes, with Chung and Ooi [32] focusing on single contact modelling and Rahman et al. [33] on bulk level modelling.

It is clear that DEM code verification and benchmarking is important, however, such studies are either not conducted or not published. One reason for this could be a lack of clear guidelines or a framework for comparing different software packages. Fig. 1 shows the scope of this paper, which is establishing a framework for comparing DEM software packages, using seemingly identical contact models and input parameter values. The aim is to investigate the portability of input parameters between different codes and to identify if software independent calibration is possible. The two packages used are EDEM Version 2021.1 by Altair and PFC Version 7 by Itasca Consulting Group.

Two contact models were used, namely the non-cohesive Hertz-Mindlin (no-slip) model, and the Edinburgh-Elasto-Plastic-Adhesion (EEPA) model. Both of these two models are available in EDEM and PFC as built-in models. However, the Hertz-Mindlin model in PFC does not include rolling resistance. Thus, for the purpose of this study, rolling resistance was added as a user-defined model. Section 2 provides the theoretical background of the two contact models and highlights the differences in implementation, and how parameter values can be scaled to obtain identical results.

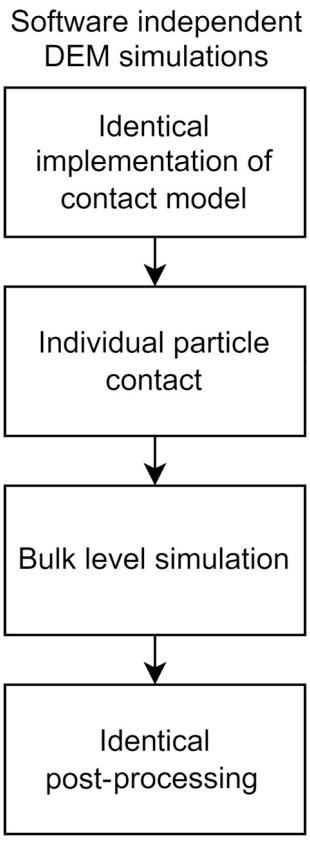

Fig. 1. Proposed framework for software independent DEM simulations.

The bulk behaviour of the material is a result of thousands of particles making contact, and identical bulk level predictions cannot be made if the behaviour at particle or contact level is different. Thus, different to existing studies, here the codes are compared at both contact level and bulk level. In Section 2.2.1 a single contact is analysed where two particles make contact in the normal and shear directions respectively. The contact between a single particle rolling down an inclined wall is also analysed. Then, in Section 2.2.2 the predictions in material bulk behaviour are compared by modelling a draw down test and comparing various measures. Lastly, the computation time to model a draw down test with varying number of particles is compared, using identical conditions and input parameter values in the two codes while using the same workstation to avoid hardware influences.

This study covers domains that can be controlled by a commercial software user, while not necessarily including the black box or 'under the hood' domain that is controlled by software developers, as shown in Fig. 2. These 'under the hood' differences are considered uncontrollable and given.

The novelty of this study is that next to benchmarks for free-flowing material by the widely used Hertz-Mindlin contact model, we also include rolling friction, and include a benchmark for the Edinburgh Elasto Plastic Adhesive (EEPA) contact model to represent cohesive materials. In addition, to the authors knowledge it is the first to compare commercial software on benchmarks. The framework provided is software agnostic and can provide a basis as well as benchmarks for future comparisons at contact and bulk levels.

2. Materials and method

2.1. Contact models

Two contact models were used in this study, namely the Hertz-

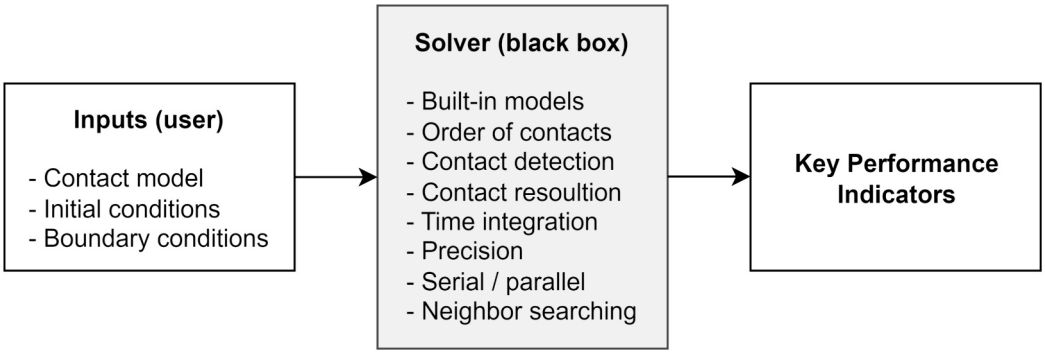

Fig. 2. Different domains influence the software dependency of DEM simulations.

Mindlin (no-slip) model and the Edinburgh-Elasto-Plastic-Adhesion (EEPA) model. Although the models are well described in literature, the basic framework is presented here and some of the implementation differences in PFC and EDEM highlighted. A rolling resistance model was also used in conjunction with the Hertz-Mindlin and EEPA models.

2.1.1. The Hertz-Mindlin contact model

The contact force in the normal direction is given by an elastic (Hertz) component F_n^H and a damping component F_n^d,

$$F_n = F_n^H + F_n^d \tag{1}$$

The normal force acts in the direction defined normal to the contact plane which is easily updated from timestep to timestep based on the contact kinematics. The contact force in the shear direction acts in a direction perpendicular to the normal and should be updated incrementally. As such, it is best presented in vector format and similar to the normal force, has an elastic and damping component,

$$\boldsymbol{F}_s = \boldsymbol{F}_s^H + \boldsymbol{F}_s^d \tag{2}$$

The formulation of the normal and shear forces is further presented below.

2.1.1.1. Elasticity in the normal direction. In the Hertz model, the force in the normal direction F_n^H between two contacting pieces is given by,

$$F_n^H = \frac{4E^*}{3R_e}a^3 \tag{3}$$

where

$$R_e = \left(\frac{1}{R_1} + \frac{1}{R_2}\right)^{-1} = \frac{R_1 R_2}{R_1 + R_2} \tag{4}$$

is the effective radius at the point of contact and R_i $(i = 1,2)$ is the radius of the two contacting bodies. With contact between a particle and a wall, the radius of the wall is taken as infinite (zero curvature), and the effective radius is equal to that of the particle. E^* is the effective Young's modulus given by,

$$E^* = \left(\frac{1-\nu_1^2}{E_1} + \frac{1-\nu_2^2}{E_2}\right)^{-1} \tag{5}$$

where E_i and ν_i are the Young's modulus and Poisson's ratio of the two contacting pieces $(i = 1, 2)$. Hertz's theory further shows that the relation between the radius a of the contact patch (assuming spherical particles and a circular contact patch) and the contact overlap δ_n in the normal direction (total deformation of the two particles at the point of contact) is given by,

$$a = \sqrt{R_e \delta_n} \tag{6}$$

Substituting this relation into Eq. (3), results in the well-known form of the Hertz contact force in the normal direction,

$$F_n^H = k_n \delta_n = \left(\frac{4}{3}E^*\sqrt{R_e\delta_n}\right)\delta_n = \frac{4}{3}E^*\sqrt{R_e}\delta_n^{\frac{3}{2}} \tag{7}$$

where the secant stiffness $k_n = \frac{4}{3}E^*\sqrt{R_e\delta_n}$ is non-linear and a function of the normal overlap δ_n. The tangent normal stiffness k_n^t, used to calculate the damping force, is given by,

$$k_n^t = \frac{\partial F_n^H}{\partial \delta_n} = 2E^*\sqrt{R_e\delta_n} = 2E^* a \tag{8}$$

2.1.1.2. Elasticity in the shear direction. The contact force vector in the shear direction F_s^H is incrementally updated,

$$\mathbf{F_s^{H^*}} = \mathbf{F_s^{H,dt-1}} + k_s^t \Delta \boldsymbol{\delta}_\mathbf{s} \tag{9}$$

where $\Delta\delta_s$ is the shear displacement increment and the tangent shear stiffness k_s^t is a function of the normal overlap δ_n,

$$k_s^t = 8G^*\sqrt{R_e\delta_n} = 8G^* a \tag{10}$$

where G^* is the effective shear modulus,

$$G^* = \left(\frac{2-\nu_1}{G_1} + \frac{2-\nu_2}{G_2}\right)^{-1} \tag{11}$$

During a given time step, the normal overlap δ_n might change, and the value at the start of the current time step is used in Eq. (10). Furthermore, the shear force is limited by the Coulomb friction condition,

$$\mathbf{F_s^H} = \begin{cases} \mathbf{F_s^{H^*}} & if\ |\mathbf{F_s^{H^*}}| \le \mu_s F_n^H \\ \mu_s F_n^H \dfrac{\boldsymbol{F}_s^{H^*}}{|\boldsymbol{F}_s^{H^*}|} & otherwise \end{cases} \tag{12}$$

where F_n^H is the Hertz normal force at the end of the current time step (Eq. (7)), and μ_s is the interface coefficient of sliding friction.

2.1.1.3. Damping in the normal direction. The viscous (dashpot) damping force in the normal direction is given by,

$$F_n^d = \begin{cases} -2\beta_n\sqrt{m_c k_n^t}\ \dot{\delta}_n & \text{PFC} \\ -2\sqrt{\frac{5}{6}}\beta_n\sqrt{m_c k_n^t}\ \dot{\delta}_n & \text{EDEM} \end{cases} \tag{13}$$

where $m_c = \frac{m_1 m_2}{m_1 + m_2}$ is the effective contact mass with m_i $(i = 1,2)$ the mass of the two particles (for particle-wall contact, the effective mass is equal to that of the particle), k_n^t is the tangent normal stiffness given by Eq. (8),

$\dot{\delta}_n$ is the relative normal translational velocity, and β_n is the critical damping ratio in the normal direction. This ratio takes a value $\beta_n = 0$ when there is no damping, and $\beta_n = 1$ when the system is critically damped.

Note the different implementation in PFC and EDEM where an additional constant $\sqrt{\frac{5}{6}} \approx 0.9129$ is introduced in the latter. For comparison purposes, the values of the critical damping ratio β_n used in the PFC models were scaled by this constant to ensure the same implementation as in the EDEM models. Furthermore, the relation between the coefficient of restitution (CoR) and the critical damping ratio is given by,

$$\beta = \frac{-ln(\mathrm{CoR})}{\sqrt{ln^2(\mathrm{CoR}) + \pi^2}} \tag{14}$$

For example, when CoR = 0.1 is reported in this text, a value $\beta = 0.591$ (Eq. (14)) was effectively used in EDEM (second condition in Eq. (13)), while a value of $\beta = 0.591\sqrt{\frac{5}{6}} = 0.539$ was used as PFC input (first condition in Eq. (13)) to ensure the same damping force.

2.1.1.4. Damping in the shear direction. The viscous damping force in the shear direction is given by the vector,

$$\mathbf{F_s^d} = \begin{cases} -2\beta_s\sqrt{m_c k_s^t}\,\dot{\boldsymbol{\delta}}_\mathbf{s} & PFC \\ -2\sqrt{\frac{5}{6}}\beta_s\sqrt{m_c k_s^t}\,\dot{\boldsymbol{\delta}}_\mathbf{s} & EDEM \end{cases} \tag{15}$$

where $\dot{\boldsymbol{\delta}}_\boldsymbol{s}$ *is* the relative shear translational velocity vector, β_s is the critical damping ratio in the shear direction, and k_s^t is the tangential shear stiffness given by Eq. (10). Here too, the value of β_s used in PFC was adjusted for the difference in implementation.

2.1.2. The EEPA contact model

This model is an extension of the linear hysteretic model by Walton and Braun [35] and was developed and first implemented by Morrissey [36] into the EDEM software package. At the time of this study, the EEPA model was not available in PFC as a build-in option. Therefore, a user-defined model was developed and implemented based on the description provided in Morrissey [36] of which some of the details were confirmed in a personal communication [37].

The contact force in the normal direction is given by the EEPA component F_n^{EEPA} and a viscous damping component F_n^d,

$$F_n = F_n^{EEPA} + F_n^d \tag{16}$$

Similarly, the contact force in the shear direction is given by (in vector notation),

$$\mathbf{F_s} = \mathbf{F_s^{EEPA}} + \mathbf{F_s^d} \tag{17}$$

The formulation of each component is further presented below.

2.1.2.1. The EEPA force in the normal direction. The model allows tensile forces to develop and also for non-linear force-displacement (overlap) behaviour as shown in Fig. 3. The load-displacement curve is defined by the constant pull-off force F_0, the loading branch stiffness k_1, the loading-unloading branch stiffness k_2, the minimum force F_{min}, the adhesion branch stiffness k_a, and the plastic overlap (deformation) δ_p. The force in the normal direction is given by,

$$F_n^{EEPA} = \begin{cases} F_0 + k_1\delta_n^m & \text{if } k_2\left(\delta_n^m - \delta_p^m\right) \geq k_1\delta_n^m \\ F_0 + k_2\left(\delta_n^m - \delta_p^m\right) & \text{if } k_1\delta_n^m > k_2\left(\delta_n^m - \delta_p^m\right) > -k_a\delta_n^\chi \\ F_0 - k_a\delta_n^\chi & \text{if } -k_a\delta_n^\chi \geq k_2\left(\delta_n^m - \delta_p^m\right) \end{cases} \tag{18}$$

Contact is activated at a normal overlap $\delta_n = 0$, where the force jumps to a value F_0 (which should take a negative value). Virgin loading follows the k_1-branch defined by the stiffness k_1 and the overlap δ_n raised to the power m (first condition in Eq. (18)). The maximum overlap δ_{max} is a history dependent parameter and is updated and stored with the contact.

Unloading follows the k_2-branch defined by the stiffness k_2 and the plastic overlap δ_p (second condition in Eq. (18)). This branch uses the same exponent m as the k_1-branch, and the stiffness k_2 is defined in terms of the plasticity ratio λ_p,

$$k_2 = \frac{k_1}{1-\lambda_p} \text{ or } \lambda_p = 1 - \frac{k_1}{k_2} \tag{19}$$

When $\lambda_p = 0$, $k_2 = k_1$ and there is no plastic behaviour, and when

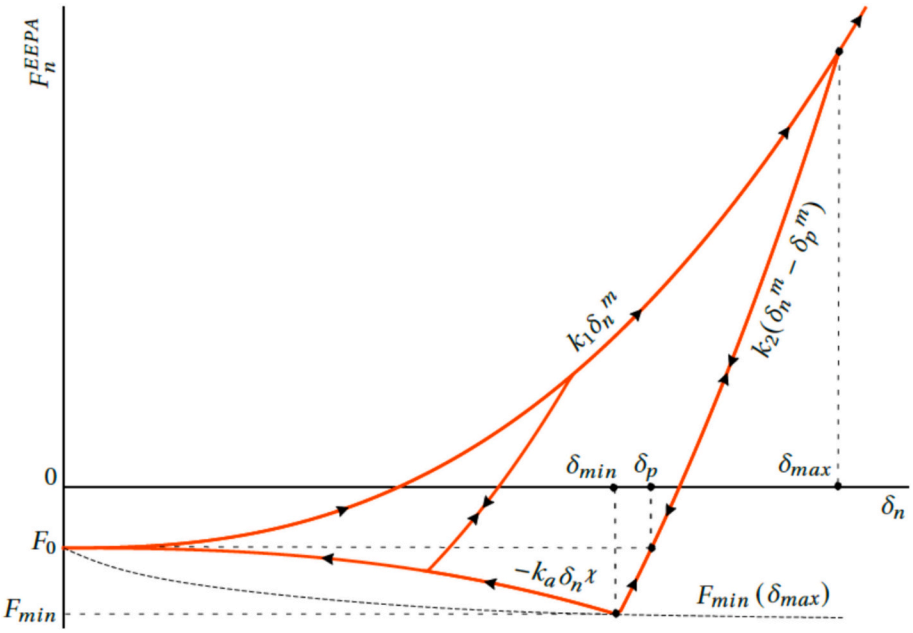

Fig. 3. EEPA model force-displacement relation in the normal direction.

$\lambda_p \to 1$, $k_2 \to \infty$ and the behaviour is perfectly plastic. The stiffness k_1 is defined in terms of the effective Young's modulus E^* (Eq. (5)), in a format similar to that of the classic Hertz model [36],

$$k_1 = \frac{4}{3} E^* \sqrt{R_e} \tag{20}$$

The plastic overlap δ_p is defined as the overlap where the force on the k_2-branch is equal to the pull-off force F_0 (and not where the force is equal to zero as indicated in the original text by [36]), and is given in terms of the maximum overlap and the plasticity ratio,

$$\delta_p = \lambda_p^{\frac{1}{m}} \delta_{max} \tag{21}$$

Unloading along the k_2-branch results in a tensile (adhesive) force, and at the plastic overlap δ_p, the force is equal to the pull-off force F_0. Further unloading follows the same branch, until the magnitude of the adhesion force is equal to the minimum force F_{min} (at $\delta_n = \delta_{min}$), which is given by,

$$F_{min} = F_0 - \frac{3}{2} \pi \gamma^* a \tag{22}$$

where γ^* is the contact effective surface adhesion energy which is based on the Johnson-Kendall-Roberts (JKR) model for adhesive forces taking van der Waals effects into account [38]. The contact patch radius (assuming a circular contact area) a is given in terms of the plastic overlap δ_p,

$$a = \sqrt{2 \delta_p R_e} \tag{23}$$

If the surface energy (γ^*) is set to zero, the adhesion branch is a horizontal line and $F_{min} = F_0$. Once the force is equal to F_{min} (at $\delta_n = \delta_{min}$) during unloading on the k_2-branch, further unloading switches to the k_a or adhesion branch (third condition in Eq. (18)). The overlap exponent (χ) and the adhesion stiffness k_a is calculated as follows, to ensure that upon further unloading on the adhesion branch, the force is equal to F_0 when $\delta_n = 0$,

$$k_a = \frac{F_0 - F_{min}}{\delta_{min}^{\chi}} \tag{24}$$

where the overlap corresponding to the minimum force is given by,

$$\delta_{min} = \left(\delta_p^m + \frac{F_0 - F_{min}}{k_2} \right)^{\frac{1}{m}} \tag{25}$$

Note that the adhesion stiffness k_a is not constant, and indirectly dependent on the load history (dependent on F_{min}, which depends on the plastic overlap δ_p, which again depends on the maximum overlap δ_{max}).

If the contact is unloading along the k_2-branch, and then starts to reload, the same k_2-branch is followed until the k_1-branch is reached. Further virgin loading follows the k_1-branch and will result in an increased and updated δ_{max} (and δ_p). If the contact is unloading along the k_a-branch, and then starts to reload, a k_2-branch is followed as shown in Fig. 1. In this case, the value of δ_p is updated to where this k_2-branch is equal to the pull-off force F_0.

On the k_2-branch, the force has a minimum limit if unloading is allowed to continue until zero overlap $\delta_n = 0$ (Fig. 1) and under some circumstances, it is possible for the unloading branch not to reach the minimum force F_{min}. The minimum force limit that can be achieved when unloading on the k_2-branch, is given by,

$$F_{min}^{limit} = F_0 - k_2 \delta_p^m \tag{26}$$

If the minimum force given by Eq. (22) is less than this limit (larger in magnitude) $F_{min} \leq F_{min}^{limit}$, the adhesion branch would never be reached and the solution for the minimum overlap δ_{min} in Eq. (25) would have no real solution. This might occur when, for example, a relatively high surface energy is specified, and a specific contact has a relatively small maximum overlap. To avoid such a situation, the minimum force F_{min} is modified and set to the average of the pull-off force F_0 and limit force F_{min}^{limit},

$$F_{min} = \begin{cases} F_0 - \frac{3}{2} \pi \gamma^* a & \text{if } F_{min} > F_{min}^{limit} \\ \frac{1}{2} \left(F_0 + F_{min}^{limit} \right) & \text{otherwise} \end{cases} \tag{27}$$

2.1.2.2. The EEPA force in the shear direction. Similar to the Hertz-Mindlin model, the shear force vector is incrementally updated,

$$\boldsymbol{F}_s^{EEPA^*} = \boldsymbol{F}_s^{EEPA,dt-1} + k_s^t \Delta \boldsymbol{\delta}_s \tag{28}$$

with the tangent shear modulus given as a function of the normal overlap [36],

$$k_s^t = k_{sf} 8 G^* \sqrt{R_e \delta_n} \tag{29}$$

where G^* is given by Eq. (11) and k_{sf} is a scaling factor for the tangential stiffness.

To account for cohesive effects in the tangential direction, the Coulomb friction limit is usually modified. This is a relatively simple approach which is easy to implement and is based on the work by Thornton [39] and Thornton and Yin [40] who showed that with adhesion present, the contact area decreases with an increase in the tangential force. The tangential force reaches a critical value, which defines the transition from a "peeling" action to a "sliding" action. Assuming the JKR theory [38], it is shown that at this critical point, the contact area corresponds to a Hertzian-like normal stress distribution under a load of $\left(F_n^H + 2F_{po}\right)$, where F_n^H is the elastic force according to Hertz's theory and F_{po} is the pull-off (maximum tensile/adhesive) force [41–43].

A similar approach is used in the EEPA model (and other cohesion/adhesion models), and the updated force from Eq. (28) is limited by the following criteria,

$$\boldsymbol{F}_s^{EEPA} = \begin{cases} \boldsymbol{F}_s^{EEPA^*} & if \left| \boldsymbol{F}_s^{EEPA^*} \right| \leq \mu_s \left(F_n^{EEPA} - F_{min} \right) \\ \mu_s \left(F_n^{EEPA} - F_{min} \right) \dfrac{\boldsymbol{F}_s^{EEPA^*}}{\left| \boldsymbol{F}_s^{EEPA^*} \right|} & otherwise \end{cases} \tag{30}$$

where the normal force F_n^{EEPA} is given by Eq. (18) and the minimum force F_{min} by Eq. (27). Note that the input value of F_{min} should be specified as negative, thus the reference force $\left(F_n^{EEPA} - F_{min}\right)$ in Eq. (30) is always larger or equal to zero.

2.1.2.3. The damping force in the normal and shear directions. The viscous (dashpot) damping force in the normal and shear directions is given by Eq. (13) and Eq. (15) respectively. However, the tangent normal stiffness k_n^t is dependent on the active contact branch,

$$k_n^t = \begin{cases} m k_1 \delta_n^{m-1} & \text{if on the } k_1 - \text{branch} \\ m k_2 \delta_n^{m-1} & \text{if on the } k_2 - \text{branch} \\ \chi k_a \delta_n^{\chi - 1} & \text{if on the } k_a - \text{branch} \end{cases} \tag{31}$$

and the tangent shear stiffness k_s^t is given by Eq. (29).

2.1.3. The rolling resistance contact model

Various rolling resistance models exist, as reviewed by Ai et al. [44]. The so-called Type C model is implemented here as also presented and promoted by Wensrich and Katterfeld [45]. The rolling resistance moment M_r is incrementally updated,

$$M_r^* = M_r^{dt-1} + k_r^t \Delta \theta_b \tag{32}$$

where k_r^t is the tangent rolling resistance stiffness and $\Delta \theta_b$ is the incre-

ment in bend-rotation and based on the contact kinematics (see PFC [46] for definition). The rolling stiffness is given by,

$$k_r^t = k_s^t R_e^2 \tag{33}$$

where k_s^t is the tangent shear stiffness given by Eq. (10) and Eq. (29) for the Hertz-Mindlin and EEPA models respectively. R_e is the effective contact radius (Eq. (4)). The up- dated moment is then checked against the friction limit,

$$\mathbf{M_r} = \begin{cases} \mathbf{M_r^*} & \text{if } \left|\mathbf{M_r^*}\right| \le \mu_r R_e \left(F_n^{EEPA} - F_{min}\right) \\ \mu_r R_e \left(F_n^{EEPA} - F_{min}\right) \left(\dfrac{\mathbf{M_r^*}}{\left|\mathbf{M_r^*}\right|}\right) & \text{otherwise} \end{cases} \tag{34}$$

where the same arguments, as used for the shear force, are used to increase the limiting moment by the effects of the cohesive force F_{min}. The normal force F_n^{EEPA} is taken at the end of the timestep and μ_r is the coefficient of rolling friction. With the rolling stiffness k_r^t proportional to the shear stiffness (Eq. (33)), it can be shown that damping is not needed in the rolling direction [45].

2.2. Simulation strategies

To compare the results of the two different software packages for the same input parameters, a series of simulation tests was developed at different levels, namely particle (or contact) level and bulk level.

2.2.1. Particle level simulations

First, simulations were undertaken at particle or contact level, which included the following:

1. The normal contact between two colliding particles
2. The shear impact between two particles
3. The rolling of a single particle on an inclined plane (wall)

The setup of each of the simulation models is described in more detail below and in each of the tests, the following key performance indicators (KPI) were recorded and used in the comparison:

1. The contact force as a function of time
2. The contact velocity as a function of time
3. The contact overlap as a function of time

while varying the following parameters:

1. The contact model (Hertz-Mindlin or EEPA)
2. The shear modulus
3. The adhesive force

2.2.1.1. Simulation A: normal contact between two colliding particles. Two equally sized spherical particles moved toward each other with an identical initial velocity $v_p = 1$ m/s, but in opposite directions as shown in Fig. 4. The gravitational acceleration was not activated, thus the particles moved with a constant velocity until contact was made. Table 1

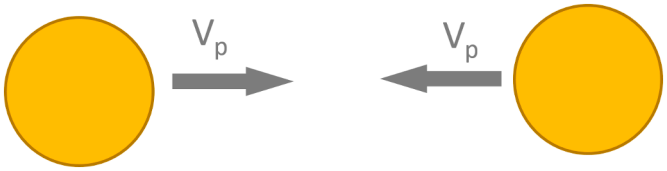

Fig. 4. Simulation A: Two spherical particles collide in normal direction with a relative velocity of 2 m/s ($v_p = 1$ m/s).

Table 1
Constant DEM input parameters in Simulation A: Normal contact between two colliding particles.

Parameter	Unit	Value
Poisson's ratio (υ)	–	0.3
Particle density (ρ_p)	kg/m^3	1000
Coefficient of sliding friction (μ_s)	–	0.1
Coefficient of rolling friction (μ_r)	–	Rotation restricted
Particle radius (R_p)	m	0.5
Time-step (Δt)	s	5e-5

provides the DEM input parameters which were kept constant, and Table 2 provides the levels of the parameters that were changed.

It is known that the rebound velocity of particles depends on the coefficient of restitution. For that reason, the influence of this coefficient on the simulation KPIs was investigated for both contact models. Also, the shear modulus was varied to compare the behaviour of the contact models for two different levels of the contact stiffness.

2.2.1.2. Simulation B: shear contact between two colliding particles. Two spherical particles collided in the shear direction, as shown in Fig. 5. The simulation setup was similar to that of Simulation A in terms of input parameters that are listed in Table 1; with three differences. Firstly, in Simulation B, to create a shear contact, the centre-to-centre distance of the two particles was $D_{p-p} = 0.99m\ (= 2R_p)$ where R_p is the particle radius. That ensured that a shear contact formed between the two particles when moving toward each other with the identical initial velocity of $v_p = 1$ m/s. Secondly, in Simulation B the shear modulus was set to a fixed value of 5 MPa, and was not varied as in Simulation A. And lastly, the Hertz-Mindlin model with the restricted rotation option was used and the coefficient of static friction was varied with three levels of 0.1, 0.3, and 0.5 to create various degrees of tangential contact force.

2.2.1.3. Simulation C: rolling of a single particle on a plane. To compare the implementation of the rolling resistance model in PFC and EDEM, a spherical particle rolling down a rigid inclined plane under the action of gravity was modelled. A particle with a radius of 5 mm was generated with its centre a distance of 17.5 mm above a horizontal plane. Testing a particle size different from those in Simulations A and B ensures that the comparative particle level analysis is not scale-variant. The component of the gravitational acceleration in the direction normal to the plane was set to $\boldsymbol{g_n} = \boldsymbol{g}{\cdot}cos(\boldsymbol{\theta})$ where $\boldsymbol{\theta}$ is the desired angle of inclination and $\boldsymbol{g}$ the magnitude of the gravitational acceleration. While keeping the component of the gravitational acceleration tangent to the plane zero, the particle dropped to the plane and through contact damping, the energy was dissipated, allowing the particle to come to rest on the plane (zero velocity). The inclination was then modelled by keeping the component of the gravitational acceleration normal to the plane unchanged, but adding a component tangent to the plane, $\boldsymbol{g_t} = \boldsymbol{g}{\cdot}sin(\boldsymbol{\theta})$, using $\boldsymbol{g} = \mathbf{9.81}$ m/s^2 and $\boldsymbol{\theta} = \mathbf{10}^{\circ}$ in this case.

Table 3 shows the constant input parameters, while the coefficient of rolling friction was varied using three levels respectively: 0, 0.1 and 0.2. The angular velocity over time was analysed as the primary KPI.

Table 2
Variable DEM input parameters in Simulation A: Normal contact between two colliding particles. Note: the value of β_s used in PFC was adjusted for the difference in implementation between EDEM and PFC ref. Eq. (13) and Eq. (15)).

Variable	Unit	Levels
Coefficient of restitution (CoR)	–	0.01, 0.10, 1.00
Contact model	–	EEPA, Hertz-Mindlin
Particle shear modulus (G)	MPa	0.5, 5

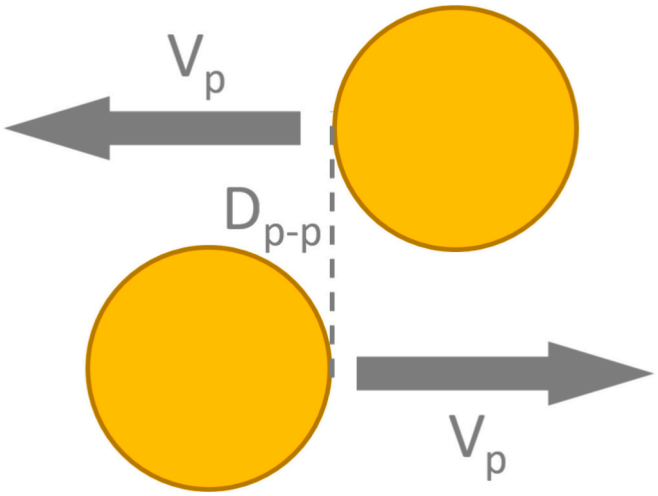

Fig. 5. Simulation B: Two spherical particles collide in the shear direction with a relative velocity of 2 m/s (v_p = 1 m/s). D_{p-p} defines the centre-to-centre distance of the two particles and equals 0.99 m here.

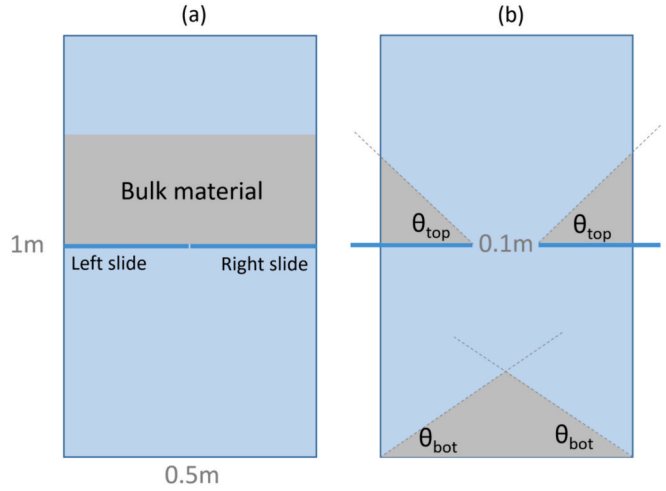

Fig. 6. Schematic view of simulation setup of draw down test; a) prior to opening slides, and b) the final condition with measurable angle of repose in both top and bottom compartments.

Table 3
Constant DEM input parameters in Simulation C: rolling of a single particle on an inclined plane.

Parameter	Unit	Value
Contact model	–	Hertz-Mindlin with rolling model C
Particle radius (R_p)	mm	5
Shear modulus (G)	MPa	100
Poisson's ratio (υ)	–	0.25
Particle density (ρ_p)	kg/m^3	3900
Sliding friction (μ_s)	–	0.2
Coefficient of restitution (CoR) and (critical damping ratio β)	–	0.1 (0.54)

2.2.2. Simulation D: bulk level

Simulations were also performed to compare the bulk behaviour as predicted by the two software packages. For this purpose, a draw down test (DDT) was used since it provides a number of bulk variables to measure, such as the angle of repose in the top and bottom compartments, the material mass in either compartment, and the material void ratio. The DDT is often used in calibration of DEM input parameters as shown by Roeplal et al. [53].

The simulation setup of the DDT is schematically shown in Fig. 6. The entire container was 1 m high, 0.5 m wide, and 0.2 m deep (out of plane). To create identical initial conditions in EDEM and PFC, particles were loosely generated in the upper compartment, first in EDEM, and before it was allowed to settle, the coordinates of each particle were exported to a text file which was imported into PFC, where the particles were then duplicated. Thereafter, the particles were allowed to settle over a period of 2.0 s, with Fig. 6a showing the static condition just prior to opening of the slides. Opening of the slides happened over a period of 0.5 s, after which the simulation was continued for a further 5.5 s to reach a static state. Fig. 6b shows the final condition, where a pile with an angle of repose of θ_{bot} was created in the bottom compartment. Also, an angle of repose of θ_{top} was created in the top compartment. The simulation was repeated at least 5 times, while following the workflow above to keep identical conditions in EDEM and PFC.

To measure the angle of repose we applied a measurement method based on that described in Mohajeri et al. [54]. Fig. 7a shows the particle configuration (position) at the end of the simulation. A grid bin is then defined as shown in Fig. 7b (not to scale) with the domain dimensions and number of bins given in Table 4 for the various measurements. All the bins containing a particle are then flagged, resulting in a binary image as shown in Fig. 7c. The area of the top angle and the bottom half of the lower angle are then isolated (Fig. 7d and e respectively). The width and height of the particle heaps are measured, and a window of interest defined using the ratios shown in Fig. 7d and e. This eliminates the rounded edges of the heap and ensures that the angle is measured where the slope is more linear. Within this window, the edge of the heap is found (using Matlab image processing and contour tools) as shown in Fig. 7d and e. Using linear regression, a straight line is fitted to the edge (contour within the window of interest) of which the slope is defined as the angle of repose (Fig. 7f and g). Although Fig. 7 shows only the measurement of the angles on the right-hand side, both the left-hand and right-hand angles were measured and then averaged. This procedure was applied to all the simulation results, ensuring consistent measurements without manual input and human influence.

In addition, the kinetic energy prior to opening the slides and the voidage in the top compartment was measured. The voidage (ε) was determined by:

$$\varepsilon = \frac{\rho_p - \rho_b}{\rho_p} \tag{35}$$

where ρ_b and ρ_p are bulk and particle density, respectively. To determine the kinetic energy density and bulk density, a grid bin is defined in the top compartment. Table 4 shows details of this grid bin. The grid bin is placed within the bulk material, which ensures that boundary surface is excluded from the density calculation.

Two distinct types of materials were modelled, including a free-flowing (non-cohesive) material and a cohesive material. The free-flowing (or non-cohesive material) material was based on iron ore pellets, as calibrated in Lommen et al. [55] using the Hertz-Mindlin contact model. Table 5 provides the main DEM input parameters of the iron ore pellets. The cohesive materials were based on moist iron ore, as calibrated in Mohajeri et al. [54] using the EEPA contact model. Table 6 provides the main input parameters of the moist iron ore. Both the free-flowing and the cohesive materials were modelled without a particle size distribution (mono-sized).

2.3. Deterministic modelling

When calculations are performed in parallel using multiple central processing units (CPUs or cores) or threads, different results can be obtained when running the same model multiple times using the same input. The reason for this is that the order of the computations (order of

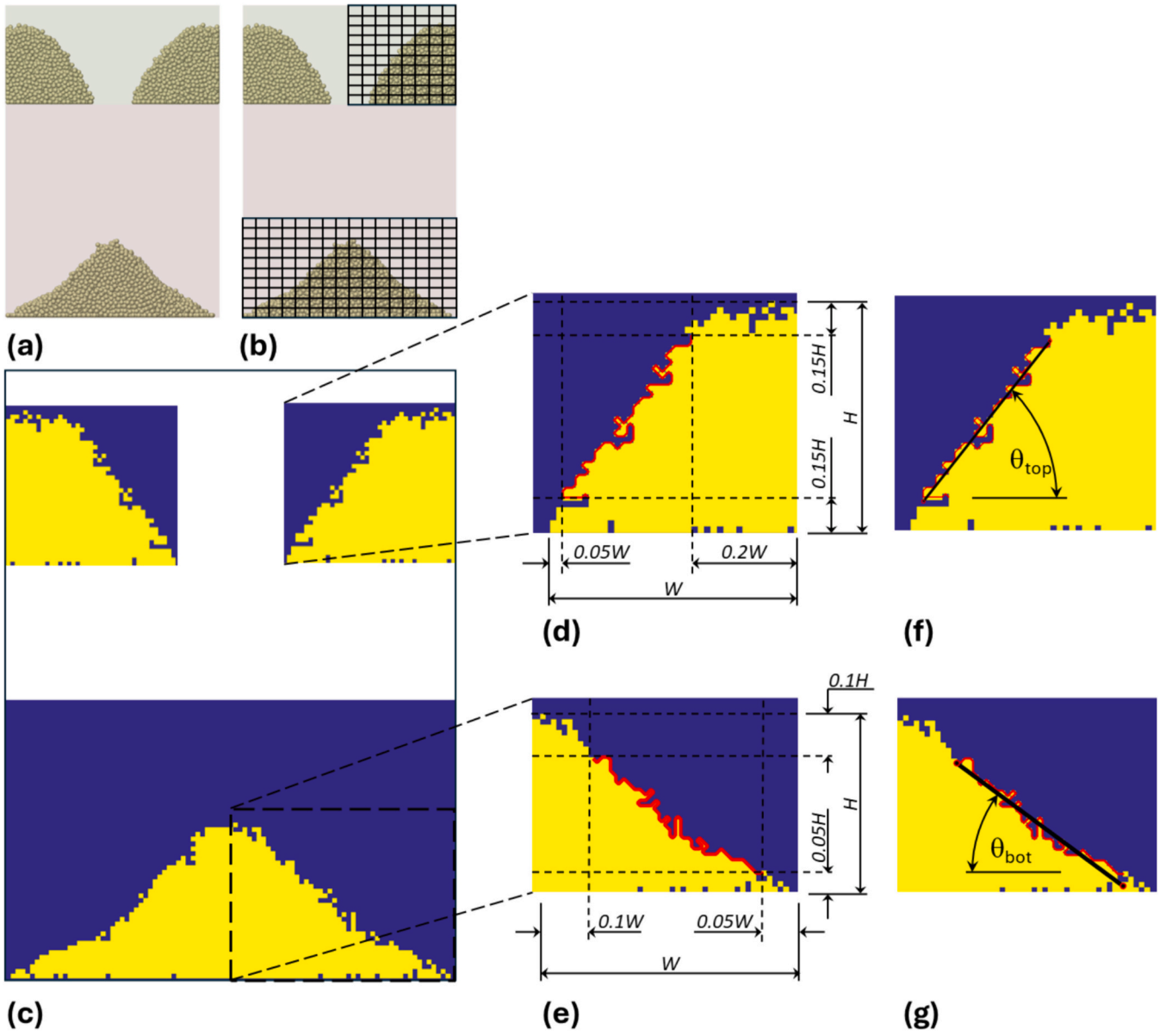

Fig. 7. Steps to measure the angles of repose: (a) particle configuration at the end of the simulation, (b) grid fitted to the model (not to scale), (c) grid-based material configuration, (d-e) the window of interest applied to the top and bottom angles respectively and finding the material edge, (f-g) fitting a straight line to the edge and measuring the top and bottom angles of repose respectively.

Table 4
Details of grid bin for measuring kinetic energy and bulk density in the top compartment of the Draw Down Test. Width and height are shown in Fig. 6.

Measure	Direction	Depth	Width	Height
Kinetic energy and bulk density	Dimension (m)	0.2	0.5	0.15
Number of bins	Number of bins	1	10	4
Top angle of repose (symmetric half)	Dimension (m)	0.05	0.25	0.2
	Number of bins	1	50	40
Bottom angle of repose (symmetric half)	Dimension (m)	0.05	0.25	0.3
	Number of bins	1	50	60

the threads or thread interleave) will differ each time that the model is executed, resulting in roundoff errors accumulating differently. The results from such a model are non-deterministic and can complicate software development and debugging. Providing customer support is also more difficult if the error cannot be duplicated by the code developer.

In a DEM model the computation difference, due to multi-threading, accumulates every timestep and can result in a different final answer with particles ending up in a slightly different position for example. All of these results are valid, and the difference per calculation is in the order of finite precision floating point error (PFC).

However, using programming methods specifically developed for this purpose, multi-threaded computations can produce identical results using a deterministic thread schedule [58]. This, however, comes at the cost of computation time. In PFC the user can select between deterministic and non-deterministic modelling, and it is estimated that the difference in computation time is approximately 15% (PFC). In EDEM, computations are deterministic, and there is not an option for users to

Table 5
Main DEM input parameters of free-flowing (dry) iron ore pellets in Simulation D, the draw down test. For a complete set of input parameters is referred to Lommen et al. [55].

Parameter	*Unit*	*Value*
Contact model	–	Hertz-Mindlin with rolling model C
Particle radius (R_p)	mm	5.5
Shear modulus (G)	MPa	100
Poisson's ratio (υ)	–	0.25
Particle density (ρ_p)	kg/m^3	3700
Coefficient of restitution (CoR), particle-particle	–	0.10
Sliding friction (μ_s), particle-particle	–	0.21
Rolling friction (μ_r), particle-particle	–	0.10
Coefficient of restitution (CoR), particle-geometry	–	0.10
Sliding friction (μ_s), particle-geometry	–	0.41
Rolling friction (μ_r), particle-geometry	–	0.10

Table 6
Main DEM input parameters of cohesive iron ore in Simulation D, the draw down test. For a complete set of input parameters is referred to Mohajeri et al. [54].

Parameter	*Unit*	*Value*
Contact model	–	EEPA
Particle radius (R_p)	mm	5.5
Shear modulus (G)	MPa	7.5
Poisson's ratio (υ)	–	0.25
Particle density (ρ_p)	kg/m^3	4500
Sliding friction (μ_s), particle-particle	–	0.31
Sliding friction (μ_s), particle-geometry	–	0.37
Coefficient of restitution (CoR)	–	0.01
Constant pull-off force (F_0)	N	−0.0025
Surface energy (γ^*)	J/m^2	8.00
Contact plasticity ratio (λ_p)	–	0.20
Loading-unloading exponential (m)	–	1.50
Adhesion exponential (χ)	–	1.50
Tangential stiffness scaling factor (k_{sf})	–	0.40

select non-deterministic modelling.

3. Results

3.1. Particle level simulations

3.1.1. Results of Simulation A: normal contact between two colliding particles

3.1.1.1. Hertz-Mindlin contact model. The outcome of Simulation A in EDEM and PFC matched perfectly. Note that the markers are purely used to indicate the different curves and do not present a data point. Fig. 8 shows the normal contact force when the Hertz-Mindlin contact model was used. Fig. 8a shows the elastic (spring) force component over time, and Fig. 8b shows the total force (elastic component plus the damping component) over the dimensionless contact overlap ($\delta n/R_p$). Varying the coefficient of restitution, affected the contact forces, with a higher coefficient of restitution resulting in a higher spring force component (Fig. 8), due to an increase in the normal overlap (Fig. 8b and Fig. 9). Also, a coefficient of restitution of 1.00 resulted in a perfectly elastic contact where no damping force component was recorded for both EDEM and PFC.

Fig. 9 shows the Hertz-Mindlin dimensionless contact overlap over time. The contact overlap was the highest at CoR = 1.0, as no damping force prevented the development of contact overlap. Fig 10 shows a particle's normal velocity over the dimensionless contact overlap. With a CoR = 1.00, a purely elastic contact was created where all the kinetic energy was transferred between the particles, therefore the magnitude of particle velocity was the same prior and after the contact, namely 1 m/s. In contrast, a CoR = 0.01 resulted in an almost perfectly plastic contact where the kinetic energy of the particle was damped; for that reason, the particle velocity dropped to almost 0 m/s.

Both EDEM and PFC were able to capture the effects of varying the coefficient of restitution on the normal contact between two spherical particles, tested with three different levels of CoR. Note that, due to the difference in implementation, the damping ratio in PFC was scaled in the results presented here as discussed in Section 2.1.1.3 (Eq. (13)). If this was not done, the results would have differed from that of EDEM and users should be aware of such seemingly small differences that can result in larger differences at the bulk level.

Next, the effects of varying particle shear modules on the normal contact between two colliding particles was tested. The results presented in Fig. 11a show the normalised overlap as a function of time, and Fig. 11b shows the elastic force component as a function of the overlap. In this model, a CoR = 0.01 was used to prevent a large overlap (i.e. larger than 1% of the particle diameter) between the two particles. A higher shear modulus (G = 5 MPa) resulted in a stiffer contact spring with a small overlap between particles, while a G = 0.5 MPa resulted in a longer contact duration and a larger overlap. Based on these results, it can be concluded that the implementation of the Herz-Mindlin model is identical in EDEM and PFC in terms of normal contact (if the damping is scaled as discussed above).

3.1.1.2. EEPA contact model. Furthermore, Simulation A was used to compare EDEM and PFC's implementation of the EEPA contact model. Fig. 12 shows that the EEPA normal contact spring force over the dimensionless contact overlap, matched between EDEM and PFC when the constant pull-off force (F_0) was set to zero. Also, the peak contact force was comparable to the simulation with the Hertz-Mindlin contact model.

Next, the constant pull-off force was set to $F_0 = -1250\,N$, to investigate if both software packages could accurately model the attractive force. As a result, as shown in Fig. 13, a constant attractive force of -1250 N was measured, which confirms the identical implementation of the EEPA contact model in EDEM and PFC.

In summary, the outcome of Simulation A is that EDEM and PFC produced identical results when a small difference in the implementation (damping ratio scale) was accounted for. This was verified for two different contact models, the Hertz-Mindlin and the EEPA model, with various levels of the coefficient of restitution, the particle shear modulus and the attractive force. Therefore, a variety of materials, ranging from free-flowing to cohesive can be simulated with EDEM and PFC using identical input parameter values and the results can be expected to be identical at contact level, i.e., software agnostic or software independent modelling.

3.1.2. Result of Simulation B: collision of two particles in the shear direction

EDEM and PFC produced identical results for the tangential force (elastic component) during shear contact for three different levels of the coefficient of static friction (Fig. 14). When the coefficient of static friction was 0.1, it took 0.034 s to reach the maximum tangential force of 202.4 N, then the tangential force dropped to zero until contact was broken. With higher levels of static friction, the contact duration was the same, while the peak force increased in magnitude for both EDEM and PFC in an identical manner. Therefore, it could be concluded that the implementation of the tangential force (and the Coulomb condition for frictional slip) is identical in EDEM and PFC.

3.1.3. Results of Simulation C: rolling of a single particle on a plane

The results from EDEM and PFC for simulation C also matched perfectly, and this shows that the implementation of the rolling resistance model (type C) is identical in both software packages. It is

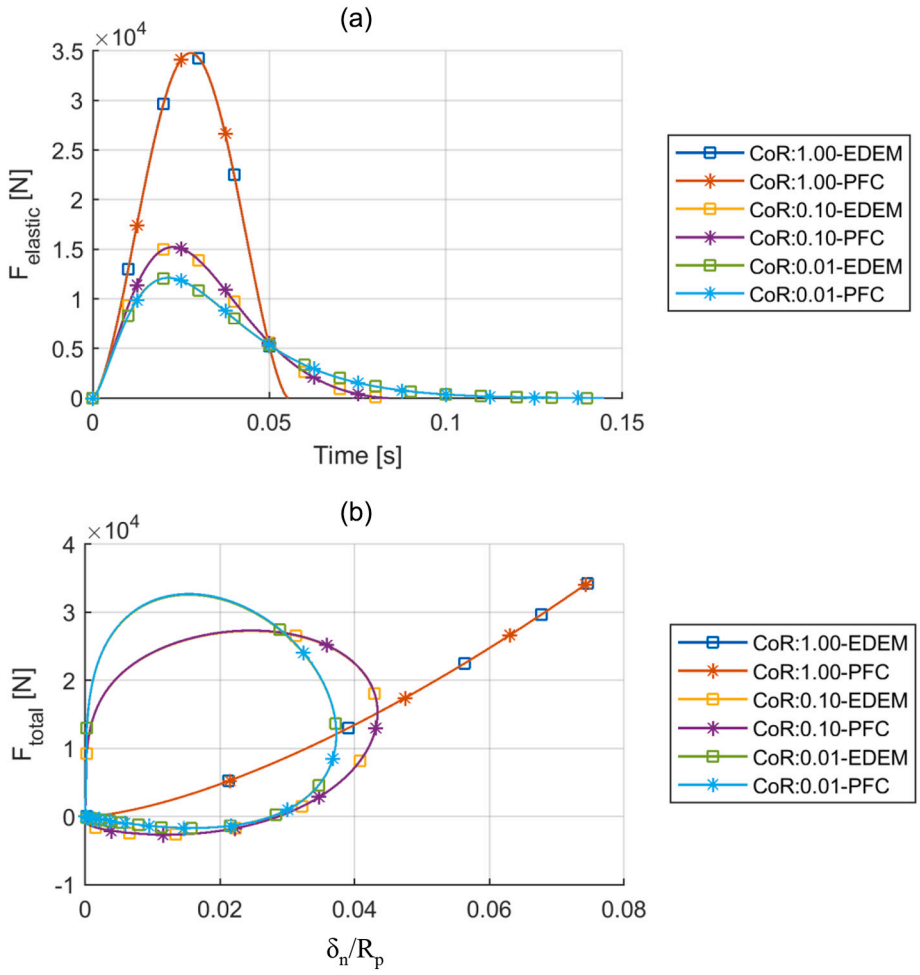

Fig. 8. Hertz-Mindlin contact force in Simulation A (normal contact between two colliding particles) with three levels of coefficient of restitution: a) contact spring force in the normal direction over time, and b) total contact force in the normal direction over the dimensionless contact overlap (δ_n/R_p).

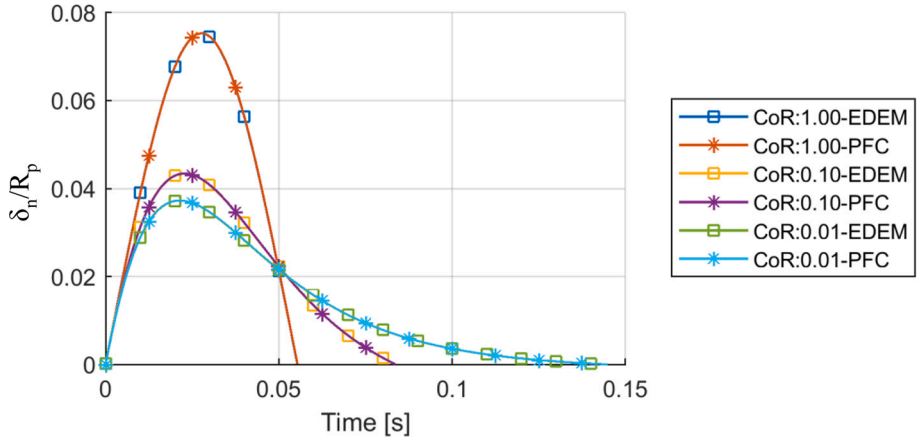

Fig. 9. Dimensionless overlap in the Hertz-Mindlin normal contact with three levels of coefficient of restitution.

important to compare this implementation since the definition of the kinematics of contact rolling between two particles can vary [44]. If the increment in rolling angle or the rolling radius are defined differently, the resistance torque will differ even if the angle-torque relation and slip condition are identically implemented.

Fig. 15 shows the angular velocity of the spherical particle with three different levels of rolling friction. When the coefficient of rolling friction was set to $\mu_r = 0$, the angular velocity increased linearly from 0 to 7000 deg./s over a period of 0.5 s in both EDEM and PFC. By increasing the coefficient of rolling friction to $\mu_r = 0.1$, the rate of change decreases by 50%, and the angular velocity at the end of simulation was equal to 3500 deg./s. Using $\mu_r = 0.2$, due to a higher rolling resistance, the spherical particle did not rotate in either EDEM or PFC. This was further analysed, and Fig. 16 shows the rolling torque at the point of contact between the particle and the geometry (wall) for the same levels of rolling friction. In both EDEM and PFC, a coefficient of rolling friction of

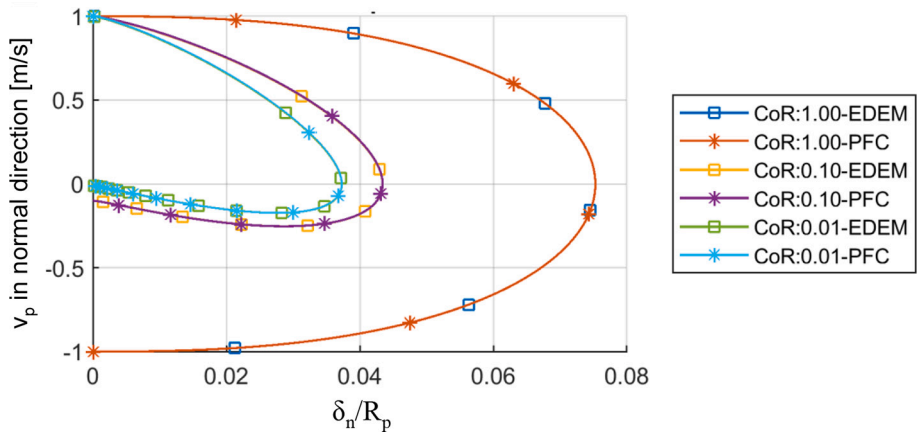

Fig. 10. Particle velocity v_p in the Hertz-Mindlin normal contact with three levels of coefficient of restitution.

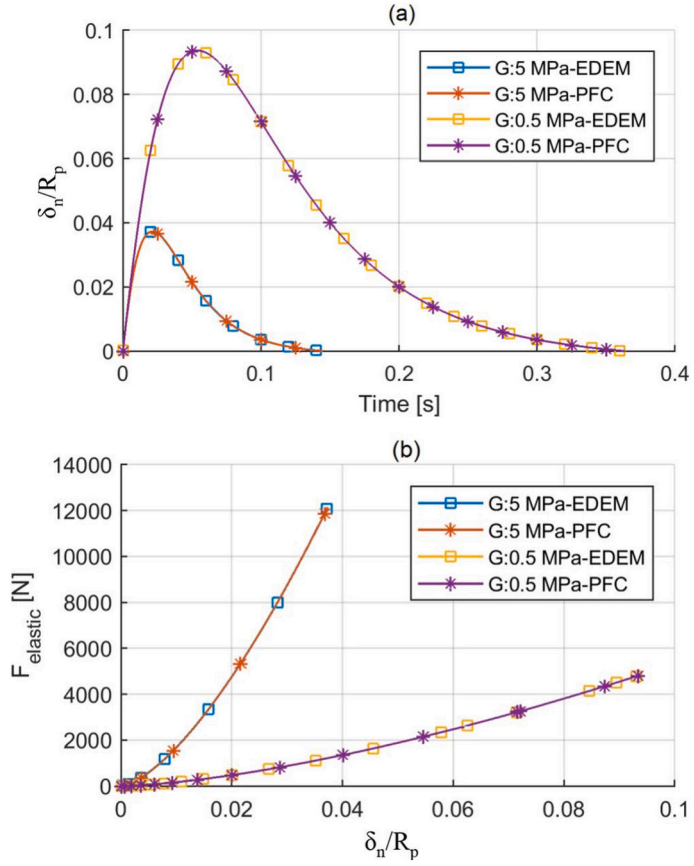

Fig. 11. Effect of varying particle shear modules in Simulation A (normal contact between two colliding particles) with the Hertz-Mindlin contact model a) dimensionless contact overlap in the normal direction over time, and b) elastic force component in the normal direction over the dimensionless contact overlap (δ_n/R_p).

$\mu_r = 0.2$ resulted in a torque of 1.74e-5 Nm once the value converged to a steady state. Note that the torque showed some small initial oscillations, corresponding to similar oscillations in the contact normal direction caused by particle settling which is damped out within the first 0.025 s. Furthermore, although the particle's rotational speed increased over time, the torque remained constant since it has no viscous (damping) component and is only dependent on the constant rotation stiffness and the effective contact radius.

3.2. Bulk level simulation

Fig. 17 illustrates the resulting piles at the end of the simulation with static piles formed in the lower compartment of the draw down model simulating cohesive behaviour using the EEPA model (top figure), and free-flowing behaviour using the Hertz-Mindlin model (bottom figure). Using the EEPA model, both EDEM and PFC were able to capture the general cohesive behaviour of the material. The profiles are not identical with some visible differences at the bottom and top of the pile for in the bottom compartment where EDEM locally shows steeper angles. Using the Hertz-Mindlin model, the general free-flowing behaviour is captured

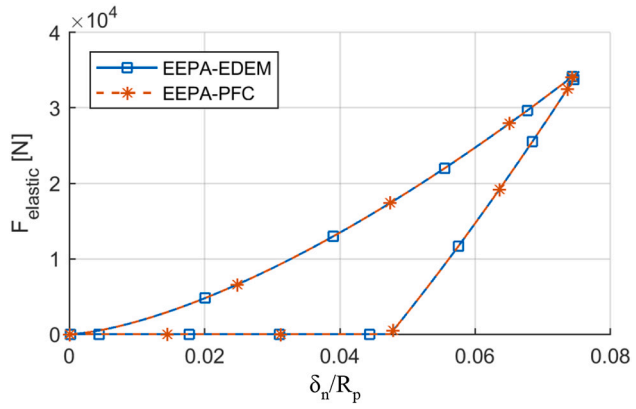

Fig. 12. EEPA contact spring force in Simulation A (normal contact between two colliding particles) without cohesive force applied.

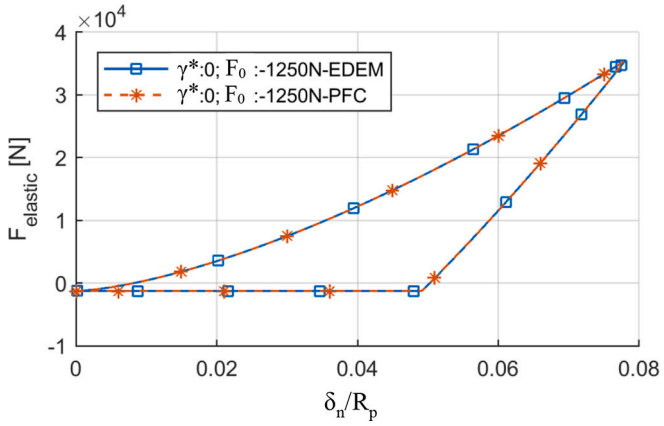

Fig. 13. EEPA contact spring force in Simulation A (normal contact between two colliding particles) without surface energy (γ^*) and with cohesive force (F_0) applied.

by both EDEM and PFC, with a higher mass in the bottom compartment with a milder angle compared to the cohesive material as expected. The angle of repose looks slightly steeper in the EDEM simulation, for both EEPA and Hertz-Mindlin models.

The results of the draw down simulations were further analysed with a summary presented in Table 7 and Table 8 for the EEPA and Hertz-Mindlin contact models respectively. Multiple results were compared, including the mass in the bottom compartment, the angle of repose in the upper compartment θ_{top} and lower compartment θ_{bot}, as well as the mean voidage and mean kinetic energy prior to opening the slides. For this comparison, deterministic modelling was used (as a check, each model was run five times, and the results were identical for each software package respectively).

When the EEPA model was used for the cohesive material, the mass in the bottom compartment was 0.54 kg higher in EDEM compared to PFC, which is only 1.2% of the total mass in the simulation. The angles of repose, θ_{top} and θ_{bot} were up to 3.91° different, with steeper angles predicted by EDEM compared to that by PFC. PFC reached a lower level of the mean kinetic energy over the same duration (2.0 s), which might be due to differences in the time integration scheme. This also resulted in a slightly higher voidage in the EDEM model. With identical results at the particle level, the bulk level simulation results showed similar but not identical results. This is expected due to the stochastic nature of granular systems and DEM modelling. Even the exact same model run twice on the same software can produce slightly different results due to multi-thread non-determinism for example [31]. However, the small differences between EDEM and PFC when using the EEPA model can all be considered small and acceptable.

When Hertz-Mindlin model was used (to simulate free flowing or non-cohesive material), the mass in the bottom compartment was 0.26 kg higher in PFC compared to EDEM, which was only 0.7% of the total mass. The mean voidage was similar between PFC and EDEM, while the angles of repose were up to 3.63° different.

In general, EDEM produced larger angles than PFC for both contact models. The top angle of repose differed by 0.5° to 1° and the bottom angle by up to almost 4°. The material that remains at the top undergoes little motion and the slope is formed by the removal of material that shears and flows away. The bottom angle of repose, however, is defined by the material forming a new heap and the particles undergo large displacement, rotation and re-positioning. Thus, it is expected that any differences in the two software packages would be more emphasised by comparing the bottom angles and not the top angles.

To answer the question on whether a difference of 4° in the angle of repose is acceptable, a number of aspects should be considered. Roessler and Katterfeld [47] reported that when repeating a simulation using the exact same parameter values and model settings, but using a newly generated sample of particles from the same PSD, the angle of repose can on average vary by ±1° (in this study it was <0.4°). Also, when physically measuring the angle, an acceptable error is <5% [48], which equates to 1° to 2° if the angle of repose is in the range of 20° to 40°.

Thus, an error in the modelled angle of repose of 2° is acceptable and considered to be accurate for bulk handling applications [17,18,49–52].

Furthermore, the results reported above were obtained by running EDEM and PFC in a deterministic mode. However, PFC was also run in non-deterministic mode, using identical input and initial particle

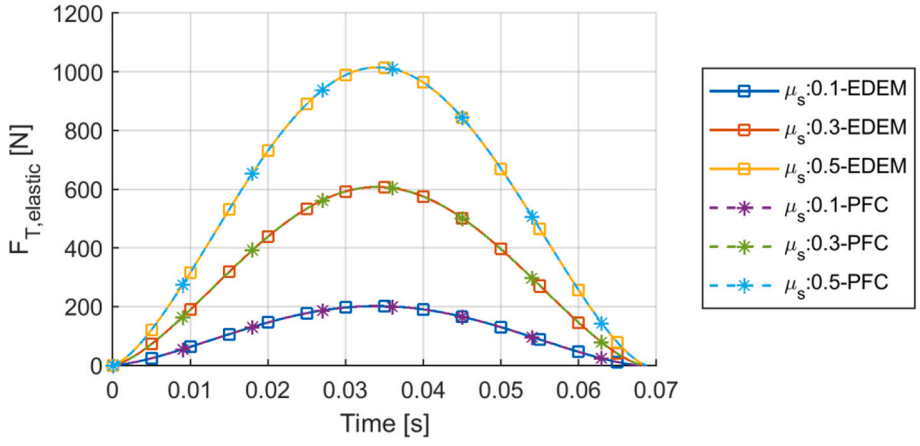

Fig. 14. Tangential force in Simulation B with three levels of static friction.

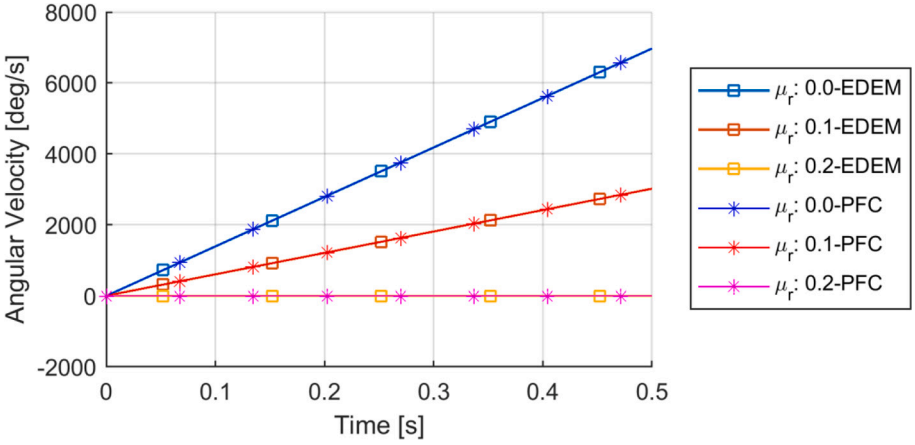

Fig. 15. Angular velocity in Simulation C with three different levels of rolling friction.

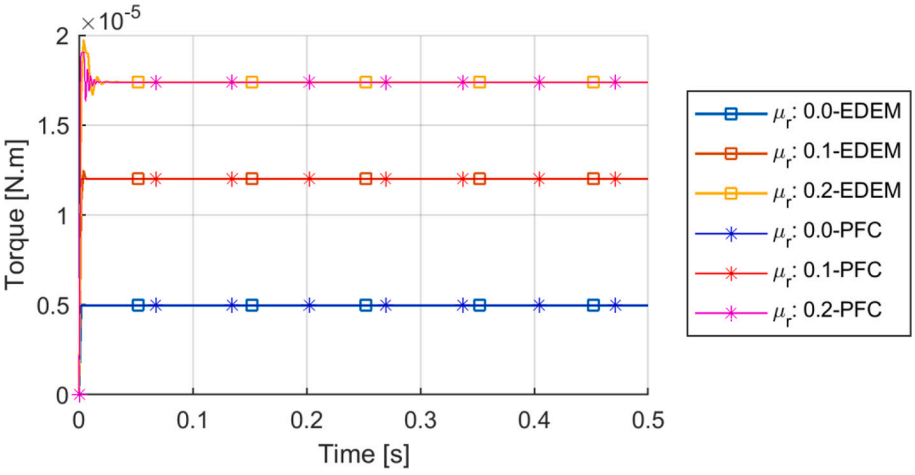

Fig. 16. Torque in Simulation C with three different levels of rolling friction

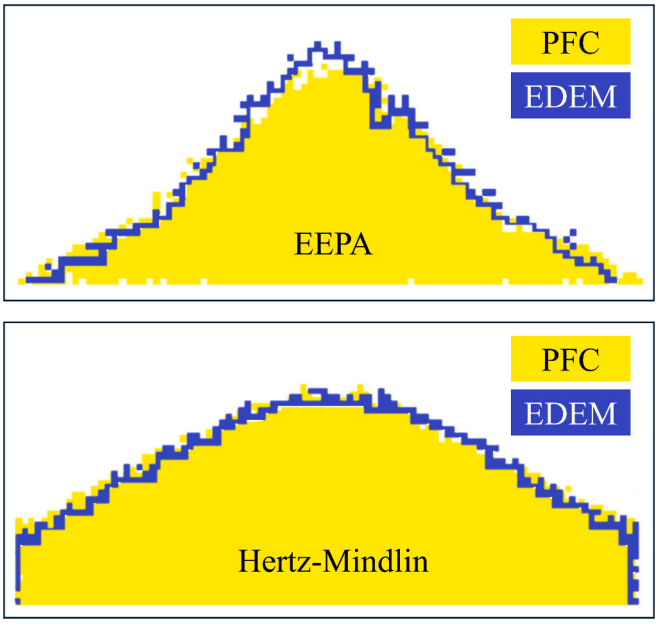

Fig. 17. Comparison of the bottom compartment of draw down simulation.

Table 7
Result of draw down deterministic simulation for EEPA contact model (5 repetitions with identical initial particle positions) for Δt = 2.0e-5 s.

EEPA Contact Model	mass in bottom compartment	mean voidage before opening (ε)	mean kinetic energy density	θ_{top}	θ_{bot}
	[kg]	[−]	[J/m^3]	[°]	[°]
PFC	19.00	45.69	1.344E-14	51.73	38.24
EDEM	19.54	46.32	2.70E-07	52.24	42.15
Difference	0.54	0.63	2.70E-07	0.51	3.91

Table 8
Results of draw down deterministic simulation for Hertz-Mindlin contact model (5 repetitions with identical initial particle positions) for Δt = 2.0e-5 s.

Hertz-Mindlin Contact Model	mass in bottom compartment	mean voidage before opening (ε)	mean kinetic energy density	θ_{top}	θ_{bot}
	[kg]	[−]	[J/m^3]	[°]	[°]
PFC	27.27	42.27	5.62E-16	25.05	25.79
EDEM	27.01	42.43	3.60E-08	26.16	29.42
Difference	0.26	0.16	3.60E-08	1.11	3.63

positions and repeated 10 times. Using the EEPA model, the average top and bottom angles of repose was 51.62° and 37.23° respectively, with standard deviations of 1.25° and 0.89°. These results are within 1° of the PFC results in deterministic mode (Table 6). However, from the ten non-deterministic runs, the difference between the maximum and minimum top and bottom angles was 4.17° and 3.03° respectively. Similarly, using the Hertz-Mindlin model, the ten simulation runs resulted in an average top and bottom angle of 23.11° and 26.58° respectively with standard deviations of 1.67° and 1.46°. The difference between the maximum and minimum angles was 5.24° and 4.92° respectively. Thus, using identical input and purely due to multi-thread non-determinism, the angle of repose can differ by as much as 4° to 5°. This also indicates that, even if all aspects of the DEM computation cycle are identically implemented, and the two software packages both make use of deterministic calculations, but follow different multi-thread scheduling, the angle of repose can differ by up to 5°. Therefore, the difference between the two software packages of almost 4° found in this study, should be considered acceptable.

On the other hand, although multi-thread non-determinism can account for the difference in results from the two packages, other differences and effects cannot be excluded. Directions for further analysis should include aspects related to solvers, as indicated in Fig. 2, but also choice of postprocessing approach. Additionally, careful representation of particle interactions at the bulk level should be considered. This can be achieved through particle interactions that account for similar velocities and cover all degrees of freedom, including torsional and shear directions.

In conclusion, with Simulation D, it could be said that with matching particle level simulations between EDEM and PFC, the bulk behaviour for both the EEPA and Hertz-MIndlin models show a certain level of similarity. Thus, if a material model is calibrated with either the Hertz-Mindlin (representing free flowing material) or EEPA models (representing cohesive material), the bulk behaviour can be considered software independent between EDEM and PFC without significant differences.

4. Discussion on the computation speed

Three particle level and one bulk level simulations were used in the previous section to compare EDEM and PFC, mainly in terms of accuracy. Additionally, the computation speed of DEM simulations is often a primary concern when simulating industrial applications with large volumes of bulk material, such as silo flow, transfer chutes, and grabs, where the number of simulated particles is often $>10^7$ [56]. In this section, the computation speed of EDEM and PFC was compared by scaling the draw down simulation.

The original scale (S = 1) of the draw down simulation, Simulation D, was used as the benchmark, with approximately 36 kg of material and 14,000 spherical particles. To scale the domain, both the top and bottom compartments were scaled in the length direction only (the original 0.5 m dimension), using scaling factors of S = 2, 4, 8, 16 and 32 with 27,000, 54,000, 108,000, 215,000 and 430,000 particles, respectively.

The total simulation time was kept constant, and the computation time was compared by analysing the minutes that it took to perform a second of simulation, as shown in Fig. 18. The computation times of EDEM and PFC3D followed a similar trend when the CPU engine was used. It took 3.6 min for PFC to simulate a second of simulation time at the original scale, while it took 4 min with EDEM (CPU). At a scale S = 32, it took 172 min to perform a second of simulation with PFC, while it took 28 min longer with EDEM (CPU). However, for the GPU engine used with EDEM, it took only 15.4 min to simulate a second of simulation with the domain scale of S = 32. Also, it took between 0.25 and 0.46 min to simulate a second of simulation per 1000 spherical particles in both EDEM and PFC3D when the CPU engine was used, as shown in Fig. 19.

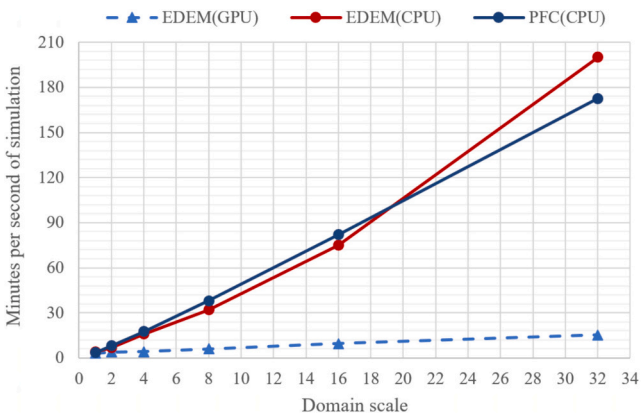

Fig. 18. Comparing the computation time of EDEM (CPU and GPU) and PFC3D (CPU) per second of simulation in various domain scales.

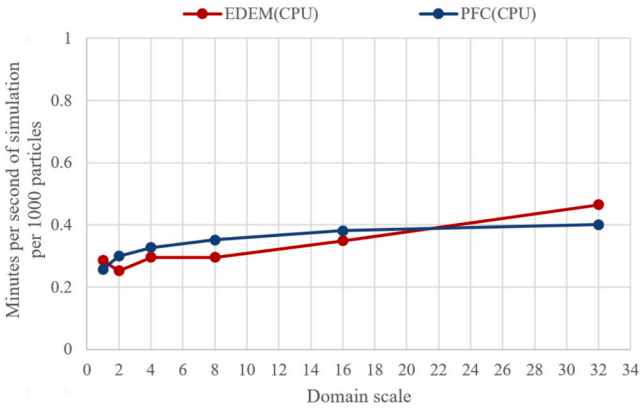

Fig. 19. Comparing the computation time of EDEM (CPU and GPU) and PFC3D (CPU) per second of simulation per 1000 spherical particles in various domain scales.

5. Conclusions

A proper framework was established to demonstrate that calibrated bulk material models can be accurately simulated using different software packages with the same input parameters. Software independent DEM simulations allow users in industry and academia to have confidence in the results, once the material model is calibrated and the input parameter values adjusted for known small differences in the specific software implementation (such as the viscous damping for example).

In this paper, software agnostic results have been demonstrated at both particle and bulk level with EDEM and PFC. By including both elastic and elasto-plastic adhesive contact models, the findings cover the entire range of bulk materials being handled in industry, ranging from free-flowing incompressible materials to cohesive compressible materials.

To compare the results, everything within the user's control to keep identical was ensured, this included initial and boundary conditions, contact model implementations, postprocessing and hardware.

With a similar implementation of contact models, particle level simulations matched between EDEM and PFC3D, in terms of head-on (normal) collision, shear collision and rolling resistance behaviour. After achieving identical results in simulations at the particle level, a calibration example using the draw down test was conducted to compare the bulk behaviour of free-flowing (non-cohesive) and cohesive materials, as simulated by EDEM and PFC respectively. The results of bulk level simulations differ but compared adequately well in terms of discharged mass into the bottom compartment, the voidage, and the angles

of repose.

Although the angles of repose from the two software packages differed by up to 4°, it was shown that multi-thread non-determinism alone can account for this. Users must understand the effects of this, and when using software that runs in a non-deterministic mode, it is advised to do multiple runs and perform a statistical analysis of the results (at least a mean and standard deviation). In general, users should use parameter values from other software packages with caution, especially where critical or sensitive applications are modelled.

The computation time between EDEM and PFC3D were similar if the simulation was done using the CPU engine. Using the GPU engine, bulk level simulations were significantly quicker; the difference between the computation time with CPU and GPU engines became larger with an increase in the number of particles. For instance, the simulation with 430,000 spherical particles was 93% faster when the GPU engine of EDEM was used, while the simulation with 14,000 spherical particles was around 50% faster than the CPU engine.

By ensuring that the DEM simulations are software independent, the calibrated material models can be used software independently, which facilitates using DEM for industrial applications and research purposes. Using novel computation techniques, such as the GPU engine, helps further to model industrial application with a practical computation time.

Next steps should include building up a benchmark framework for robust and generalized DEM material models, where both open source and commercial codes should be included to leverage the work of all (future) DEM users both in engineering practice and academia.

CRediT authorship contribution statement

M. Javad Mohajeri: Writing – original draft, Visualization, Validation, Methodology, Investigation, Formal analysis, Data curation, Conceptualization. **Corné Coetzee:** Writing – review & editing, Writing – original draft, Software, Methodology, Investigation, Formal analysis, Conceptualization. **Dingena L. Schott:** Writing – review & editing, Supervision, Resources, Project administration, Methodology, Formal analysis, Conceptualization.

Declaration of competing interest

The authors declare that they have no known competing financial interests or personal relationships that could have appeared to influence the work reported in this paper.

Data availability

Data will be made available on request.

References

[1] M.J. Mohajeri, A.J. van den Bergh, J. Jovanova, D.L. Schott, Systematic design optimization of grabs considering bulk cargo variability, Adv. Powder Technol. 32 (5) (2021) 1723–1734.

[2] M.P. Fransen, M. Langelaar, D.L. Schott, Application of DEM-based metamodels in bulk handling equipment design: methodology and DEM case study, Powder Technol. 393 (2021) 205–218.

[3] J. Rossow, C.J. Coetzee, Discrete element modelling of a chevron patterned conveyor belt and a transfer chute, Powder Technol. 391 (2021) 77–96, https://doi.org/10.1016/j.powtec.2021.06.012. Elsevier B.V.

[4] A. Katterfeld, T. Donohue, D. Ilic, Application of the discrete element method in mechanical conveying of bulk materials, in: 07th International Conference for Conveying and Handling of Particulate Solids. Friedrichshafen, Germany, 2012.

[5] D. Ilic, A. Roberts, C. Wheeler, Modelling bulk solid interactions in transfer chutes: accelerated flow, Chem. Eng. Sci. 209 (2019) 115197, https://doi.org/10.1016/j.ces.2019.115197. Elsevier Ltd.

[6] M.J. Mohajeri, W. de Kluijver, R.L.J. Helmons, C. van Rhee, D.L. Schott, A validated co-simulation of grab and moist iron ore cargo: replicating the cohesive and stress-history dependent behaviour of bulk solids, Adv. Powder Technol. 32 (4) (2021) 1157–1169, https://doi.org/10.1016/j.apt.2021.02.017.

[7] D. Schott, J. Mohajeri, J. Jovanova, S. Lommen, W. de Kluijver, Design framework for DEM-supported prototyping of grabs including full-scale validation, J. Terrramech. 96 (2021) 29–43.

[8] E. Yazdani, S.H. Hashemabadi, The influence of cohesiveness on particulate bed segregation and mixing in rotating drum using DEM, Physica A 525 (2019) 788–797, https://doi.org/10.1016/j.physa.2019.03.127.

[9] G. Basinskas, M. Sakai, Numerical study of the mixing efficiency of a batch mixer using the discrete element method, Powder Technol. 301 (2016) 815–829, https://doi.org/10.1016/j.powtec.2016.07.017.

[10] G.W. Delaney, R.D. Morrison, M.D. Sinnott, S. Cummins, P.W. Cleary, DEM modelling of non-spherical particle breakage and flow in an industrial scale cone crusher, Miner. Eng. 74 (2015) 112–122, https://doi.org/10.1016/j.mineng.2015.01.013.

[11] C. Coetzee, O.C. Scheffler, Comparing particle shape representations and contact models for DEM simulation of bulk cohesive behaviour, Comput. Geotech. 159 (2023) 105449.

[12] U.T. Hoang, N.H.T. Nguyen, Particle shape effects on granular column collapse using superquadric DEM, Powder Technol. 424 (2023) 118559, https://doi.org/10.1016/j.powtec.2023.118559.

[13] Y.T. Feng, Thirty years of developments in contact modelling of non-spherical particles in DEM : a selective review, Acta Mech. Sinica 39 (2023) 722343.

[14] U.T. Hoang, N.H.T. Nguyen, Particle shape effects on granular column collapse using superquadric DEM, Powder Technol. 424 (2023) 118559, https://doi.org/10.1016/j.powtec.2023.118559.

[15] A.P. Herman, Z. Zhou, J. Gan, Y. Aibing, Scaling up studies for mixing of granular materials in rotating drums, Powder Technol. 403 (2022) 117408, https://doi.org/10.1016/j.powtec.2022.117408.

[16] S. Lommen, D. Schott, G. Lodewijks, DEM speedup: stiffness effects on behavior of bulk material, Particuol. Chin. Soc. Particuol. 12 (1) (2014) 107–112, https://doi.org/10.1016/j.partic.2013.03.006.

[17] T. Roessler, C. Richter, A. Katterfeld, F. Will, Development of a standard calibration procedure for the DEM parameters of cohesionless bulk materials – part I: solving the problem of ambiguous parameter combinations, Powder Technol. 343 (2019) 803–812, https://doi.org/10.1016/j.powtec.2018.11.034.

[18] C. Richter, T. Rössler, G. Kunze, A. Katterfeld, Development of a standard calibration procedure for the DEM parameters of cohesionless bulk materials – part II: efficient optimization-based calibration, Powder Technol. 360 (2020) 967–976, https://doi.org/10.1016/j.powtec.2019.10.052. Elsevier B.V.

[19] C.J. Coetzee, Review: calibration of the discrete element method, Powder Technol. 310 (2017) 104–142, https://doi.org/10.1016/j.powtec.2017.01.015. Elsevier B.V.

[20] N. Govender, R. Kobyłka, J. Khinast, The influence of cohesion on polyhedral shapes during mixing in a drum, Chem. Eng. Sci. 270 (2023) 118499.

[21] G. Sutmann, Classical molecular dynamics, in: J. Grotendorst, D. Marx, A. Muramatsu (Eds.), Quantum Simulations of Complex Many-Body Systems: From Theory to Algorithms, NIC Series, vol. 10, John von Neumann Institute for Computing, Julich, 2002, pp. 211–254.

[22] T. Reinikainen, T. Welo, A.S. Korhonen, A. Kivivouri, Comparison of two commercial FEM codes in cold extrusion simulation, J. Mater. Process. Technol. 42 (1994) 137–146.

[23] M.A. Porter, D.H. Martens, A comparison of the stress results from several commercial finite element codes with ASME section VIII, division 2 requirements 336, 1996, pp. 341–346.

[24] M.A. Porter, D.H. Martens, C.S. Hsieh, A comparison of finite element codes and recommended investigation methodology, ASME 359 (1997) 241–246.

[25] X. Tan, W. Chen, J. He, T. Wang, G. Chen, H. He, Benchmark solutions for the dynamic analysis of general rotor-bearing system with arbitrary linear boundary conditions, Appl. Math. Model. 118 (2023) 709–727.

[26] S.M. Roberts, F.R. Hall, A. Van Bael, P. Hartley, I. Pillinger, C.E.N. Sturgess, P. Van Houtte, E. Aernoudt, Benchmark tests for 3-D, elasto-plastic, finite-element codes for the modelling of metal forming processes, J. Mater. Process. Technol. 34 (1–4) (1992) 61–68.

[27] Jörg Schröder, Thomas Wick, Stefanie Reese, Peter Wriggers, Ralf Müller, Stefan Kollmannsberger, Markus Kästner, Alexander Schwarz, Maximilian Igelbüscher, Nils Viebahn, Hamid Reza Bayat, Stephan Wulfinghoff, Katrin Mang, Ernst Rank, Tino Bog, Davide D'Angella, Mohamed Elhaddad, Paul Hennig, Alexander Düster, Wadhah Garhuom, Simeon Hubrich, Mirjam Walloth, Winnifried Wollner, Charlotte Kuhn, Timo Heister, A selection of benchmark problems in solid mechanics and applied mathematics, Arch. Computat. Methods Eng. 28 (2021) 713–751.

[28] H. Saomoto, N. Kikkawa, S. Moriguchi, Y. Nakata, M. Otsubo, V. Angelidakis, Y. P. Cheng, K. Chew, G. Chiaro, J. Duriez, S. Duverger, J.I. Gonzalez, M. Jiang, Y. Karasaki, A. Kono, X. Li, Z. Lin, A. Liu, S. Nadimi, H. Nakase, D. Nishiura, U. Rashique, H. Shimizu, K. Tsuji, T. Watanabe, X. Xu, M. Zeghal, Round robin test on angle of repose: DEM simulation results collected from 16 groups around the world, Soils Found. 63 (2023) 101272.

[29] J.M.F.G. Holst, J.M. Rotter, J.Y. Ooi, G.H. Rong, Numerical modelling of silo filling. II: discrete element analyses, J. Eng. Mech. 125 (1999) 104–110.

[30] C. Ramirez-Aragin, J. Ordieres-Mere, F. Alba-Elias, A. Gonzalez-Marcos, Comparison of cohesive models in EDEM and LIGGHTS for simulating powder compaction, Materials 11 (2018) 2341.

[31] M. Dosta, D. Andre, V. Angelidakis, R.A. Caulk, M.A. Celigueta, B. Chareyre, J.-F. Dietiker, J. Girardot, N. Govender, C. Hubert, R. Kobylka, A.F. Moura, V. Skorych, D.K. Weatherley, T. Weinhart, Comparing open-source DEM frameworks for simulations of common bulk processes, Comput. Phys. Commun. 296 (2024) 109066.

[32] Y.C. Chung, J.Y. Ooi, Benchmark tests for verifying discrete element modelling codes at particle impact level, Granul. Matter 13 (2011) 643–656.
[33] M. Rahman, D.L. Schott, A. Katterfeld, C. Wensrich, Influence of the software on the calibration parameters for DEM simulations, Bulk Solids Handl. 7 (8) (2011) 396–400.
[34] J. Salomon, C. O'Sullivan, F. Patino-Ramirez, On data benchmarking and verification of discrete granular simulations, Data Brief 53 (2024) 110252.
[35] O.R. Walton, R.L. Braun, Viscosity, granular-temperature, and stress calculations for shearing assemblies of inelastic, frictional disks, J. Rheol. 30 (5) (1986) 949–980.
[36] J.P. Morrissey, Discrete Element Modelling of Iron Ore Pellets to Include the Effects of Moisture and Fines, PhD thesis, University of Edinburgh, Edinburgh, Scotland, 2013.
[37] J. Morrisey, Personal communication, June, 2020.
[38] K.L. Johnson, K. Kendall, A.D. Roberts, Surface energy and the contact of elastic solids, Proc. Roy. Soc. Lond. Ser. A 324 (1558) (Sept. 1971) 301–313.
[39] C. Thornton, Interparticle sliding in the presence of adhesion, J. Phys. D. Appl. Phys. 24 (11) (1991) 1942–1946, https://doi.org/10.1088/0022-3727/24/11/007. ISSN 13616463.
[40] C. Thornton, K.K. Yin, Impact of elastic spheres with and without adhesion, Powder Technol. 65 (1–3) (1991) 153–166, https://doi.org/10.1016/0032-5910(91)80178-L. ISSN 00325910.
[41] J.S. Marshall, Discrete-element modeling of particulate aerosol flows, J. Comput. Phys. 228 (5) (2009) 1541–1561, https://doi.org/10.1016/j.jcp.2008.10.035.
[42] J.S. Marshall, Q.L. Shuiqing, Adhesive Particle Flow: A Discrete-Element Approach, Cambridge University Press, New York, New York, 2014.
[43] J. Hærvig, U. Kleinhans, C. Wieland, H. Spliethoff, A.L. Jensen, K. Sørensen, T. J. Condra, On the adhesive JKR contact and rolling models for reduced particle stiffness discrete element simulations, Powder Technol. 319 (2017) 472–482, https://doi.org/10.1016/j.powtec.2017.07.006. ISSN 1873328X.
[44] J.F. Ai, J.M. Chen, Rotter, and J. Y. Ooi., Assessment of rolling resistance models in discrete element simulations, Powder Technol. 206 (2011) 269–282, https://doi.org/10.1016/j.powtec.2010.09.030.
[45] C.M. Wensrich, A. Katterfeld, Rolling friction as a technique for modelling particle shape in DEM, Powder Technol. 217 (2012) 409–417, https://doi.org/10.1016/j.powtec.2011.10.057. ISSN 00325910.
[46] PFC, Version 6.0. www.itascacg.com, 2021.
[47] T. Roessler, A. Katterfeld, Scaling of the angle of repose test and its influence on the calibration of DEM parameters using upscaled particles, Powder Technol. 330 (2018) 58–66.
[48] I.S. Ferreira, R.S. Peruchi, N.J. Fernandes, P. Rotella Junior, Measurement system analysis in angle of repose of fertilizers with distinct granulometries, Meas. J. Int. Meas. Confed. 170 (2021) 108681.
[49] P. Aela, L. Zong, M. Esmaeili, M. Siahkouhi, G. Jing, Angle of repose in the numerical modeling of ballast particles focusing on particle dependent specifications: parametric study, Particuology 65 (2022) 39–50.
[50] G.K. Barrios, R.M. de Carvalho, A. Kwade, L.M. Tavares, Contact parameter estimation for DEM simulation of iron ore pellet handling, Powder Technol. 248 (2013) 84–93.
[51] W. Chen, A. Roberts, A. Katterfeld, C. Wheeler, Modelling the stability of iron ore bulk cargoes during marine transport, Powder Technol. 326 (2018) 255–264.
[52] M. Rackl, K.J. Hanley, A methodical calibration procedure for discrete element models, Powder Technol. 307 (2017) 73–83.
[53] R. Roeplal, Y. Pang, A. Adema, J. van der Stel, D. Schott, Modelling of phenomena affecting blast furnace burden permeability using the discrete element method (DEM)–a review, Powder Technol. 118161 (2022).
[54] M.J. Mohajeri, C. van Rhee, D.L. Schott, Replicating cohesive and stress-history-dependent behavior of bulk solids: feasibility and definiteness in DEM calibration procedure, Adv. Powder Technol. 32 (5) (2021) 1532–1548.
[55] S. Lommen, M. Mohajeri, G. Lodewijks, D. Schott, DEM particle upscaling for large-scale bulk handling equipment and material interaction, Powder Technol. 352 (2019) 273–282.
[56] M.J. Mohajeri, R.L. Helmons, C. van Rhee, D.L. Schott, A hybrid particle-geometric scaling approach for elasto-plastic adhesive DEM contact models, Powder Technol. 369 (2020) 72–87.
[58] H. Cui, J. Wu, J. Gallagher, H. Guo, J. Yang, Efficient deterministic multithreading through schedule relaxation, in: OSP'11, October 23–26, Cascais, Portugal, 2011.

Further-reading

[57] PFC (computer software), Particle Flow Code, Version 7, Itasca Consulting Group, 2024. www.itascacg.com.